Tailoring magnetism in self-intercalated $Cr_{1+\delta}Te_2$ epitaxial films

Y. Fujisawa,[1] M. Pardo-Almanza,[1] J. Garland,[1,2] K. Yamagami,[1] X. Zhu,[1] X. Chen,[3] K. Araki,[4] T. Takeda,[4] M. Kobayashi,[4,5] Y. Takeda,[6] C. H. Hsu,[7] F. C. Chuang,[7] R. Laskowski,[8] K. H. Khoo,[8] A. Soumyanarayanan,[3,9] and Y. Okada[1]

[1]*Quantum Materials Science Unit, Okinawa Institute of Science and Technology (OIST), Okinawa 904-0495, Japan*
[2]*Applied Physics & Mathematics Department, Northeastern University, Boston, Massachusetts 02115, USA*
[3]*Institute of Materials Research and Engineering, Agency for Science Technology and Research, 138634 Singapore*
[4]*Department of Electrical Engineering and Information Systems, The University of Tokyo, 7-3-1 Hongo, Bunkyo-ku, Tokyo 113-8656, Japan*
[5]*Center for Spintronics Research Network, The University of Tokyo, 7-3-1 Hongo, Bunkyo-ku, Tokyo 113-8656, Japan*
[6]*Materials Sciences Research Center, Japan Atomic Energy Agency, Sayo, Hyogo 679-5148, Japan*
[7]*Department of Physics, National Sun Yat-sen University, Kaohsiung 80424, Taiwan*
[8]*Institute of High Performance Computing, Agency for Science, Technology and Research, 138632 Singapore*
[9]*Department of Physics, National University of Singapore, 117551 Singapore*

(Received 25 May 2020; revised 1 August 2020; accepted 20 August 2020; published 4 November 2020)

Magnetic transition metal dichalcogenide (TMD) films have recently emerged as promising candidates in hosting novel magnetic phases relevant to next-generation spintronic devices. However, systematic control of the magnetization orientation, or anisotropy, and its thermal stability characterized by Curie temperature (T_C), remains to be achieved in such films. Here we present self-intercalated epitaxial $Cr_{1+\delta}Te_2$ films as a platform for achieving systematic/smooth magnetic tailoring in TMD films. Using a molecular-beam epitaxy based technique, we have realized epitaxial $Cr_{1+\delta}Te_2$ films with smoothly tunable δ over a wide range (0.33–0.82), while maintaining NiAs-type crystal structure. With increasing δ, we found monotonic enhancement of T_C from 160 to 350 K, and the rotation of magnetic anisotropy from out-of-plane to in-plane easy-axis configuration for fixed film thickness. Contributions from conventional dipolar and orbital moment terms are insufficient to explain the observed evolution of magnetic behavior with δ. Instead, *ab initio* calculations suggest that the emergence of antiferromagnetic interactions with δ, and its interplay with conventional ferromagnetism, may play a key role in the observed trends. This demonstration of tunable T_C and magnetic anisotropy across room temperature in TMD films paves the way for engineering different magnetic phases for spintronic applications.

DOI: 10.1103/PhysRevMaterials.4.114001

I. INTRODUCTION

Epitaxial thin films and heterostructures have provided pristine platforms for exploring different functionalities and phenomena [1,2]. Meanwhile, the concomitant development of material "knobs" to tailor these properties is key to exploit them for technological applications [3,4]. For example, the development of magnetic thin films for high-performance memory applications has required systematic modulation of the magnetic anisotropy—which sets the device geometry and switching characteristics—and enhancement of the temperature scale governing magnetic stability [5,6]. Recently, magnetic anisotropy has also served as an important knob in realizing exotic topological states in thin films [7–11], wherein practical considerations also require efforts to achieve magnetic stability beyond room temperature [9]. These efforts motivate the development of epitaxial thin-film platforms wherein the magnetic properties may be smoothly modulated, and also serve the search for novel magnetic states.

Recent intensive studies point to transition metal chalcogenides (TMDs) as one of the most promising platforms to realize such tunable characteristics [12,13]. $Cr_{1+\delta}Te_2$ in particular is a unique self-intercalated TMD—expected to have rich magnetic properties based on bulk investigations [14–26]. Previous studies of bulk crystals grown with varying compositions, e.g., CrTe [14–16], Cr_3Te_4 [17], Cr_2Te_3 [18,26], Cr_5Te_8 [19–22], and $CrTe_2$ [23–25]—were shown to have the same NiAs-type structure with ferromagnetic transition temperature (T_C) ranging between 170 and 350 K. The notation $Cr_{1+\delta}Te_2$ conveniently represents the compositions of all these compounds, wherein δ is the fraction of Cr atoms self-intercalated between neighboring $CrTe_2$ layers [see Fig. 1(a)]. Notably, in addition to conventional ferromagnetic (FM) interaction, $Cr_{1+\delta}Te_2$ bulk crystals are suggested to host antiferromagnetic (AF) interactions, noncollinear spin textures, and tunable magnetic anisotropy [27–30]. Meanwhile, epitaxial thin-film growth has focused on Cr_2Te_3(001) due to its perpendicular magnetic anisotropy with $T_C \sim 170$ K [31–35], and recent studies have suggested the presence of emergent topological phenomena in ultrathin Cr_2Te_3 films or interfaces [34,36–38]. However, the absence of means to systematically control δ has constrained a deeper understanding of underlying magnetic interactions in $Cr_{1+\delta}Te_2$, and limited the potential for engineering magnetic phases. Notably, the

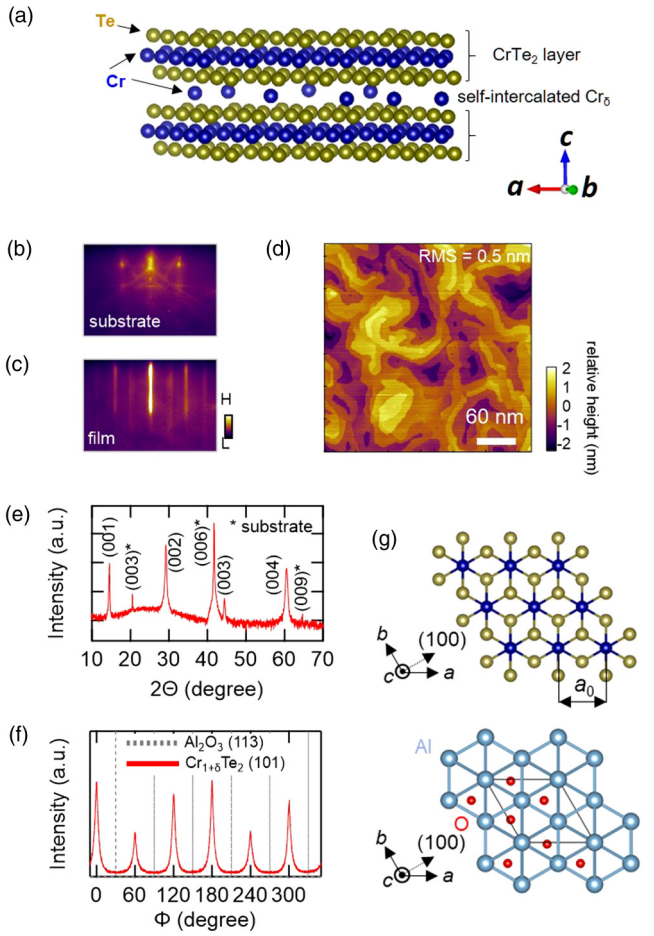

FIG. 1. Epitaxial growth of as-grown $Cr_{1+\delta}Te_2$ film. (a) Side view of crystal structure of $Cr_{1+\delta}Te_2$ showing intercalation of Cr_δ between $CrTe_2$ layers forming NiAs structure. (c) RHEED patterns for Al_2O_3 substrate, taken just before film deposition at 300 °C, and for as-grown film, taken at room temperature. The electron beam is injected along (100) direction of Al_2O_3 substrate. (d) STM topography (set bias: 200 mV; feedback current: 200 pA), with the root-mean-square (rms) value of surface roughness indicated. (e) XRD profile along (00L) orientation of the as-grown film. (f) XRD φ scans with respect to asymmetric peaks: (101) of $Cr_{1+\delta}Te_2$ (red) and (113) of Al_2O_3 (gray). (g) Relative epitaxial orientation between substrate and film in this study.

intrinsically high vapor pressure of Te (and other chalcogens in general) has limited efforts to vary δ over a wide enough range using conventional epitaxial film growth methods.

Here, we establish a method to realize epitaxial $Cr_{1+\delta}Te_2$ films with smoothly modulated δ over a wide range (0.33–0.82), while maintaining the same crystal structure, using a molecular-beam epitaxy (MBE) based growth technique. We successfully tuned the Curie temperature T_C from 160 K to above 350 K, and the magnetic anisotropy smoothly between out-of-plane (OP) and in-plane (IP) easy axes. Our calculations suggest that the modulation of magnetic properties originates from the introduction of AF interactions due to self-intercalated Cr atoms, and their interplay with conventional FM. This establishes $Cr_{1+\delta}Te_2$ as a promising epitaxial platform to investigate unconventional magnetic phases.

II. METHODS

The films were grown using molecular-beam epitaxy (MBE) equipment, whose base pressure was $\sim 10^{-10}$ Torr. Cr and Te were evaporated using an *e*-beam evaporator and a *K* cell. An electron-beam gun and screen were equipped to check the surface quality of the sample. The $Cr_{1+\delta}Te_2$ films were deposited on Al_2O_3 substrates with an area of approximately $3 \times 4\,mm^2$. Regarding the detail growth sequence, see the followings and the Supplemental Material [39].

In situ STM observation was carried out at 10 K using ultrahigh vacuum STM. Films were transferred from the MBE chamber to the STM chamber without exposing films to the air, using an ultrahigh vacuum suitcase with its base pressure of 10^{-10} Torr. In order to get electric contact between the film and bias electrodes for STM observation, Ti and Pt were deposited on the edge of Al_2O_3 substrate before MBE thin-film growth.

The x-ray-diffraction measurements were performed at room temperature and ambient pressure using Bruker D8 Discover. Cu-$K\alpha 1$ ($\lambda = 1.5418$ nm) was used as the x-ray source. The measurements were done at room temperature. The lattice constant c_0 was estimated from XRD profiles along the (00L) direction, while (101) diffraction was used to estimate the lattice constant a_0. After calculating d_{101} from these data, a_0 was calculated from d_{101} and c_0 based on the hexagonal symmetry of crystals (see Fig. S2 of the Supplemental Material [39]).

The chemical composition was determined based on EDS measurement using FEI Quanta 250 FEG. To protect against surface degradation, before all *ex situ* measurements shown in this paper, films were capped with an amorphous Se layer at room temperature with 50–100-nm thickness after cooing the sample for more than 10 h.

DC magnetization measurements were performed using a magnetic property measurement system (MPMS®3, Quantum Design).

First-principles DFT calculations were performed using the WIENNCM package that employs linearized augmented plane waves (LAPW) as a basis set [40–44]. R_{kmax} was set to 7.5 for the energy cutoff and the Brillouin zone was sampled using a $19 \times 19 \times 11$ $\boldsymbol{k}$-point grid. The exchange-correlation was obtained using the Perdew-Burke-Ernzerhof parametrization of generalized gradient approximation [45]. We considered two structures in our calculations, $CrTe_2$ ($\delta = 0$) and CrTe ($\delta = 1$), having $P6_3/mmc$ and $P3m1$ space-group symmetries respectively. The atomic structures and lattice constants were relaxed using collinear magnetic configurations with a force component cutoff of 0.01 eV/Å. The magnetic exchange interactions were then calculated using the frozen magnon approach, with spin spirals generated on a $15 \times 15 \times 9$ $\boldsymbol{q}$-point grid using the generalized Bloch theorem and a spin spiral angle of $\pi/4$. The total energies obtained from these calculations give the exchange coupling in $\boldsymbol{q}$ space, $J(\boldsymbol{q})$, and these can be Fourier transformed to generate exchange couplings in real space, $J(\boldsymbol{R})$.

III. EXPERIMENTAL RESULTS

The growth of epitaxial $Cr_{1+\delta}Te_2$ films with different δ on Al_2O_3 (001) substrate was achieved by following a two-step procedure using molecular-beam epitaxy (MBE):

(i) preparation of as-grown $Cr_{1+\delta}Te_2$ films with fixed δ, and (ii) additional *in situ* postdeposition annealing (iPDA) to tune δ. First, we describe the procedure used to prepare as-grown epitaxial films. We began by preparing a clean, atomically flat Al_2O_3 (001) substrate surface whose quality is verified using reflection high-energy electron diffraction (RHEED) [Fig. 1(b)]. $Cr_{1+\delta}Te_2$ films were then deposited at a substrate temperature of 300 °C, with as-grown film thickness consistently kept to ∼80 nm in this work. An atomically flat surface with negligible roughness on the as-grown film was confirmed by sharp RHEED streaks [Fig. 1(c)] and an *in situ* scanning tunneling microscope (STM) topographic image [Fig. 1(d)]. Notably, the stoichiometric composition of the as-grown film was found to be $\delta = 0.33$ using *ex situ* energy dispersive x-ray spectroscopy (EDS) characterization. The *ex situ* structural characterization using x-ray diffraction (XRD), shown for the (00L) direction, did not indicate the presence of any impurity phases [Fig. 1(e)]. Furthermore, based on an azimuthal XRD scan [Fig. 1(f)], the epitaxial nature of the films was confirmed by establishing the crystallographic orientation of the film relative to the substrate [Fig. 1(g)].

iPDA enables systematic control of the high volatility element—Te in our case—while keeping the film surface atomically flat [46–49]. The iPDA process involves annealing the as-grown film under adequate flow of Te flux for 30 min at a substrate temperature (T_A). In this work, T_A was varied between 300 and 700 °C for different iPDA sequences while keeping all other growth parameters unchanged (see the Supplemental Material for details [39]). Figure 2(a) shows the *ex situ* XRD profiles for films with iPDA at varying T_A values. For samples with T_A ranging over 400–600 °C, all peaks can be indexed by either substrate or $Cr_{1+\delta}Te_2$ (00L). Meanwhile, samples with $T_A = 650$ and 700 °C showed additional peaks identified as originating from a pure Cr phase [arrows in Fig. 2(a)]. While the $Cr_{1+\delta}Te_2$ (003) peak is proximate to the additional Cr(210) peak, systematic investigation of EDS and XRD data enables a clear disentanglement of these two peaks (see the Supplemental Material for more details [39]). Thus, we conclude that $T_A \sim 650$ °C corresponds to the temperature above which the film may degrade into a multiple crystalline phase. Importantly, for T_A below ∼650 °C, the relation between T_A and δ, determined from EDS, indicates a monotonic and smooth increase [Fig. 2(b)]. Based on the empirical $\delta(T_A)$ relation, we conclude that near-complete CrTe (δ∼1) can be obtained between 525 °C and 600 °C. Here the decrease of (003) peak intensity can be explained by the extinction rule for ideal CrTe ($\delta = 1$) with NiAs-type crystal structure—where the (003) peak cannot exist [50]. Meanwhile, the (003) peak may be prominent for smaller δ when the crystal structure has two inequivalent layers (see the Supplemental Material for details [39]). In summary, our iPDA technique realizes systematic tuning of δ while maintaining the crystal structure of the as-grown $Cr_{1+\delta}Te_2$ film.

Structural characterization further indicates the monotonic change of lattice parameters with varying δ. Figure 2(c) shows the δ dependence of lattice constant along IP (a_0) and OP (c_0), as well as the unit volume $V_0 (= \frac{\sqrt{3}}{2} a_0^2 c_0)$. Importantly, based on Vegard's law [51], the linear relation between lattice parameters and δ confirms the systematic change in the self-intercalation of Cr atoms between neighboring $CrTe_2$ layers

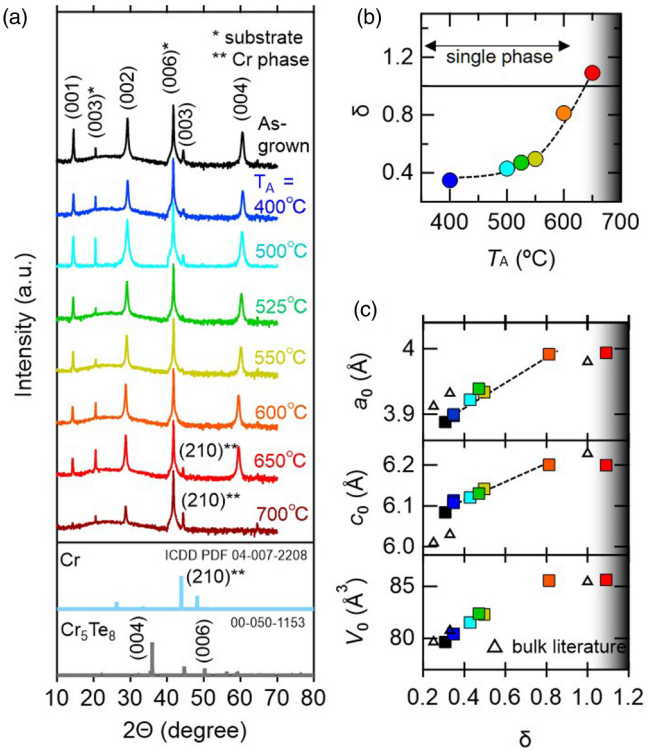

FIG. 2. Structural and compositional characterization after *in situ* postdeposition annealing with varying temperature (T_A). (a) XRD intensity profiles along (00L) direction for varying TA, vertically offset for clarity. * and ** indicate diffraction peaks originating from substrate and pure Cr, respectively. Lower graph shows referential powder-diffraction patterns of pure Cr and Cr_5Te_8 ($\delta = 0.25$) taken from ICDD Database. (b) Scanning electron microscope–EDS measurements of variation of δ as a function of T_A. The dashed parabolic trendline is a guide to the eye. (c) Variation of lattice constants a_0 and c_0 and unit-cell volume V_0 as a function of δ, determined from XRD measurements. Dashed lines show a fit to Vegard's law. Triangular symbols indicate corresponding parameters for bulk crystals from literature [14,16,19].

[see Fig. 1(a)]. Finally, we compare the values of a_0 and c_0 for our films with literature on bulk crystals with similar δ [Fig. 2(c), upper panel]. We find that our films have a slightly elongated a_0 and correspondingly shorter c_0 compared to bulk crystals [14,16,19]—resulting in a similar unit-cell volume [Fig. 2(c)]. This points to the existence of a finite IP tensile strain in our films, which could modify the electronic and magnetic properties with respect to bulk crystals.

The controlled stoichiometric variation within $Cr_{1+\delta}Te_2$ films should produce measurable effects on the magnetic properties—investigated here using magnetization (M) measurements—across temperatures $M(T)$ [Fig. 3(a)] and external fields $M(H)$ [Fig. 3(b)]. First, we present the δ dependence of the T_C by examining field-cooled ($H = 1000$ Oe) $M(T)$ curves along IP (blue) and OP (red) orientations. As seen clearly in Fig. 3(a) across both IP and OP $M(T)$ curves, T_C increases monotonically with δ. The systematic evolution of T_C with δ is summarized in Fig. 3(c) (left axis): smoothly increasing from ∼160 K for $\delta = 0.33$ [top in Fig. 3(a)] up to ∼350 K for $\delta = 0.82$ [bottom in Fig. 3(a)]. This is

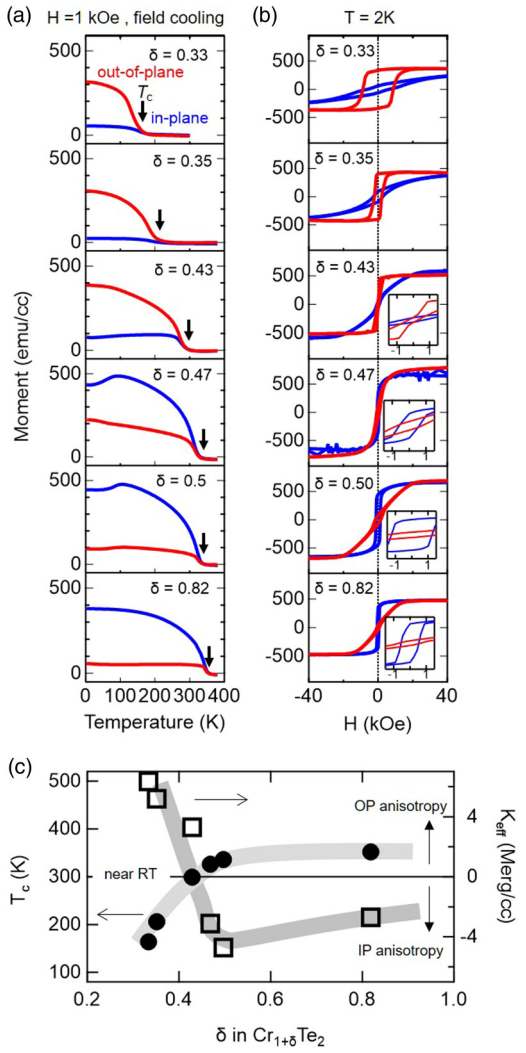

FIG. 3. Evolution of magnetic properties for $Cr_{1+\delta}Te_2$ films ($0.3 < \delta < 0.82$). Magnetization as a function of temperature, acquired by field cooling (FC) with a 1000-Oe magnetic field (H). Red and blue lines indicate data taken with H along out-of-plane (OP) and in-plane (IP) configurations, respectively. The Curie temperature T_C is indicated by an arrow. (b) Magnetization hysteresis curves at 2 K for each δ, acquired in OP (red) and IP (blue) configurations, respectively. The diamagnetic signal from substrate is subtracted in (b). The effective magnetic anisotropy K_{eff} was calculated from areal difference of IP and OP $M(H)$ loops [52]. (c) The δ dependence of T_C (left axis, filled circle) and K_{eff} (right axis, empty square). Thick lines in (c) are guides to the eye for T_C and K_{eff}.

a demonstration of systematically tunable T_C across room temperature.

More interestingly, we also see a systematic evolution of magnetic anisotropy with δ. The anisotropy change is evident from the change in remnant magnetization of the IP and OP $M(T)$ curves around $\delta = 0.4$ samples [Fig. 3(a)]. For a quantitative picture, we turn to $M(H)$ hysteresis curves acquired across δ at $T = 2$ K in IP and OP configurations [Fig. 3(b)]. For each δ, the effective anisotropy (K_{eff}) is determined by the areal difference between the IP and OP $M(H)$ curves [52]. The variation of K_{eff} with δ is summarized in Fig. 3(d) (left axis) and is consistent with the expected trend from $M(T)$ curves in Fig. 3(a). For $\delta = 0.4$ and below, K_{eff} is positive which signifies OP, or perpendicular magnetic anisotropy. However, K_{eff} reduces with increasing δ and changes sign across $\delta \sim 0.4$, resulting in IP magnetic anisotropy for $\delta > 0.4$.

Typically sample shape and magnetocrystalline (or uniaxial) contributions play major roles in determining magnetic anisotropy [51]. Here we examine the expected contributions from these two effects. First, shape anisotropy originates from magnetostatic, or dipole interactions, which for thin films leads to preferential IP anisotropy. However, such effects are consistent across δ, and therefore cannot describe the observed evolution with δ (see the Supplemental Material [39]). Meanwhile, magnetocrystalline contributions arise from the atomic-orbital moments. To examine this effect, we performed x-ray magnetic circular dichroism (XMCD) measurements at the Cr $L_{2,3}$ edge, and find that the orbital moment is negligibly small and does not vary measurably with δ (see the Supplemental Material [39]) [53–57]. Thus, neither of the conventional anisotropy contributions—shape or uniaxial—can explain the observed anisotropy switching with δ.

IV. THEORETICAL CALCULATIONS

To elucidate the physics governing the observed doping evolution of magnetism in $Cr_{1+\delta}Te_2$ films, we performed DFT calculations [46–49] for the stoichiometric compounds with $\delta = 0$ and $\delta = 1$, i.e., $CrTe_2$ [Figs. 4(a) and 4(c)] and CrTe [Figs. 4(b) and 4(d)]. The exchange interactions for these compounds were calculated using the frozen magnon method [39]. Within this technique, real-space exchange couplings are determined from the Fourier transform of the k-space dispersion of spin spirals (see Sec. II and the Supplemental Material for details [39]). Importantly, while $\delta = 0$ ($CrTe_2$) has only one Cr atom per unit cell, $\delta = 1$ (CrTe) has two Cr sublattices within its basis [Figs. 4(a) and 4(b)]. Thus, for $\delta = 0$, we have only one relevant interaction—the intrasublattice exchange interaction J_{11} [green arrows in Fig. 4(a)]. In contrast, $\delta = 1$ has two distinct intrasublattice exchange interactions J_{11} and J_{22} and additionally, an *intersublattice* exchange interaction J_{12} [red arrows in Fig. 4(b)]. From inspecting Fig. 4(b), we conclude that the two intrasublattices for $\delta = 1$ are physically indistinguishable, and therefore J_{11} and J_{22} should behave similarly. As a consistency check, we find that our DFT calculations correctly reproduce this similarity [Fig. 4(d)], and are also in line with previous calculations for individual dopings [21–24].

Figures 4(c) and 4(d) compare the spatial decay of the three intra- and one intersublattice exchange interactions for $\delta = 0,1$ respectively. First, a comparison of the intrasublattice interactions shows that J_{11} and J_{22} ($\delta = 1$) are identical, and show very similar spatial decay to J_{11} ($\delta = 0$). This may be associated with a $\sim$+5 meV nearest-neighbor FM interaction—expected to be consistent across δ [Figs. 4(c) and 4(d)]. Meanwhile, the intersublattice exchange J_{12} arises in $\delta = 1$ from the addition of a full doping layer and contrasts strongly with the radial profiles of J_{11} and J_{22}. Crucially, J_{12} shows a mix of FM and AF interactions—evolving from strongly negative (−10 meV) for the nearest neighbor to moderately positive (+3 meV) for next-nearest neighbor, highlighted by a shaded pink line in Fig. 4(d). Taken together,

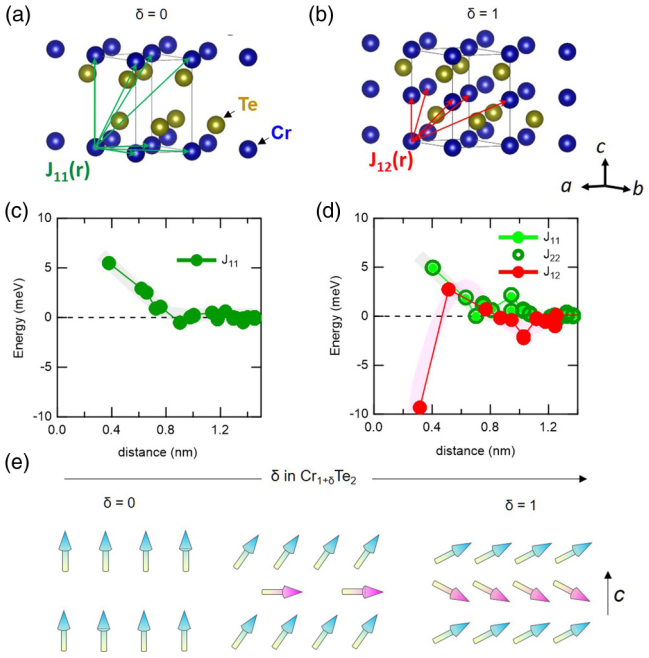

FIG. 4. Calculated exchange interactions for $Cr_{1+\delta}Te_2$ ($\delta = 0,1$). (a),(b) Crystal structures of $CrTe_2$ ($\delta = 0$) and CrTe ($\delta = 1$). Green and red arrows indicate direct exchange interactions for pairs of atoms in intrasublattice (J_{11}) and intersublattice (J_{12}) configurations. For simplicity, (b) does not show green arrows for the two distinct intrasublattice contributions J_{11} and J_{22} that are included in the calculation for CrTe [see (d)]. (c),(d) DFT-calculated exchange interactions J_{11}, J_{22}, and J_{12} as a function of atomic separation for $\delta = 0$ (c) and 1 (d) as per the structures in (a) and (b) respectively. Thick lines in (c) and (d) are guides to the eye for distance evolution for J_s. (e) Cartoon showing expected evolution of ground-state magnetic configuration of $Cr_{1+\delta}Te_2$ with varying δ, with individual arrows indicating the local orientation of magnetization.

the DFT results for $\delta = 0,1$ suggest a competition between the AF nearest-neighbor intersublattice $J_{12} = -10$ meV, FM intrasublattice $J_{11} = J_{22} = +5$ meV and next-nearest-neighbor intersublattice $J_{12} = +3$ meV interactions. The interplay of these interactions is vital to explaining the observed evolution of magnetic properties.

Next, we proceed to compare the experimental and DFT results to elucidate the doping evolution of magnetism in $Cr_{1+\delta}Te_2$. First, the calculated exchange interactions, under the random-phase approximation (RPA), give Curie temperatures $T_C = 357$ K for $\delta = 0$ ($CrTe_2$) and $T_C = 491$ K for $\delta = 1$ (CrTe). These results are qualitatively consistent with the experimental trend. In this light, the monotonic enhancement of T_C with doping [Fig. 3(b)] can be understood to result from the increased effective exchange field strength at Cr sites due to additional intersublattice interactions J_{12} with intercalated Cr atoms [58]. The effective exchange field is determined by summing up exchange interactions from all neighboring sites. Furthermore, the experimentally observed anisotropy evolution with δ may also be interpreted in view of the calculated exchange interactions. Figure 4(e) shows a possible schematic for the doping evolution of alignment of local moments in $Cr_{1+\delta}Te_2$. While moments in the original layers are aligned FM [light-blue arrows in Fig. 4(e)], those in the self-intercalated layer [pink arrows in Fig. 4(e)] tend to align AF with respect to the original layers—which could result in noncollinearity. Indeed, such noncollinearity is consistent with our calculations (Fig. S7 [39]), and is also seen in previous literature, especially in high δ compounds [28,29]. The noncollinear state in Fig. 4(e) provides a viable explanation of the observed doping evolution of anisotropy. This picture also supports the observation of coercive hysteresis for both IP and OP orientations across the entire doping range $0.33 < \delta < 0.82$, which suggests the existence of net moments within both orientations [Fig. 3(c)].

The tunable magnetism realized within our $Cr_{1+\delta}Te_2$ films provides a promising platform for burgeoning efforts in topological magnetism [36–38]. Modulating δ alters not only the spacing between self-intercalated Cr atoms, but also the Fermi-surface volume and geometry. This provides a rich playground for magnetic interactions, including direct FM and AF exchange, superexchange, and Ruderman-Kasuya-Kittel-Yosida (RKKY) interactions leading to qualitatively different intra- and intersublattice exchange couplings. Interestingly, competition between direct FM exchange and higher-order AF exchange interactions in Pd/Fe/Ir(111) [59] and RKKY-like interactions in Gd_2PdSi_3 [60] is expected to stabilize magnetic skyrmions. Recently much excitement has centered around using the interfacial Dzyaloshinskii-Moriya interaction (iDMI) to generate topological spin textures in magnetic thin films. Consequently, magnetic TMD films are being engineered to similarly achieve iDMI [8,9,36–38]. In contrast, our work shows that epitaxial $Cr_{1+\delta}Te_2$ films may host other interesting competing Interactions that may lead to other emergent ground states.

V. SUMMARY

In summary, we have established a growth technique to controllably vary the fraction of self-intercalated Cr atoms within epitaxial $Cr_{1+\delta}Te_2$ films while maintaining the original crystal structure. Consequently, we have realized tunable magnetism—including T_C beyond room temperature and smooth modulation of magnetic anisotropy between OP and IP configurations. These effects are expected to arise from the interplay of FM and AF interactions between Cr atoms and bode well for the imminent applicability of epitaxial $Cr_{1+\delta}Te_2$ films.

ACKNOWLEDGMENTS

The crystal structures of $Cr_{1+\delta}Te_2$ were visualized using VESTA [61]. This work was partly supported by Japan Society and Science and Technology Agency (JST) Core Research for Evolution Science and Technology (CREST), Japan, Grant No. JPMJCR18I2. This work was also partially supported by the Spintronics Research Network of Japan (Spin-RNJ). Supporting experiments at SPring-8 were performed under the Shared Use Program of JAEA Facilities (Proposal No. 2019B-E20) with the approval of Nanotechnology Platform project supported by the Ministry of Education, Culture, Sports, Science and Technology (Proposal No. A-19-AE-0040). The synchrotron radiation experiments were performed at JAEA beamline BL23SU in SPring-8 (Proposal

No. 2019B3841). The work in Singapore was supported by the SpOT-LITE program (Grant No. A18A6b0057), funded by Singapore's RIE2020 initiatives. We acknowledge the support of the National Supercomputing Centre (NSCC), Singapore, for computational resources. We are grateful for the help and support provided by the Engineering Support Section of Research Support Division at OIST. CHH and FCC acknowledge the support from the National Center for Theoretical Sciences and the Ministry of Science and Technology of Taiwan under Grant No. MOST-107-2628-M-110-001-MY3. CHH and FCC are also grateful to the National Center for High-Performance Computing for computer time and facilities.

[1] A. Manchon, H. C. Koo, J. Nitta, S. M. Frolov, and R. A. Duine, Nat. Mater. **14**, 871 (2015).
[2] F. Hellman, A. Hoffmann, Y. Tserkovnyak, G. S. D. Beach, E. E. Fullerton, C. Leighton, A. H. MacDonald, D. C. Ralph, D. A. Arena, H. A. Durr, P. Fischer, J. Grollier, J. P. Heremans, T. Jungwirth, A. V. Kimel, B. Koopmans, I. N. Krivorotov, S. J. May, A. K. Petford-Long, J. M. Rondinelli *et al.*, Rev. Mod. Phys. **89**, 025006 (2017).
[3] A. Soumyanarayanan, N. Reyren, A. Fert, and C. Panagopoulos, Nature (London) **539**, 509 (2016).
[4] D. Akinwande, C. Huyghebaert, C. H. Wang, M. I. Serna, S. Goossens, L. J. Li, H.-S. Wong, and F. H. L. Koppens, Nature (London) **573**, 507 (2019).
[5] J. K. Slauhter, Annu. Rev. Mater. Res. **39**, 277, (2019).
[6] D. Apalkov, B. Dieny, and J. M. Slaughter, Proc. IEEE **104**, 1797 (2016).
[7] N. Nagaosa and Y. Tokura, Nat. Nanotechnol. **8**, 899 (2013).
[8] J. Matsuno, N. Ogawa, K. Yasuda, F. Kagawa, W. Koshibae, N. Nagaosa, Y. Tokura, and M. Kawasaki, Sci. Adv. **2**, e1600304 (2016).
[9] A. Soumyanarayanan, M. Raju, A. L. G. Oyarce, A. K. C. Tan, M - Y. Im, A. P. Petrovic, P. Ho, K. H. Khoo, M. Tran, C. K. G M, F. Ernult, and C. Panagopoulos, Nat. Mater. **16**, 898 (2017).
[10] Y. Ohuchi, J. Matsuno, N. Ogawa, Y. Kozuka, M. Uchida, Y. Tokura, and M. Kawasaki, Nat. Commun. **9**, 213 (2018).
[11] M. Nakamura, D. Morikawa, X. Yu, F. Kagawa, T. Arima, Y. Tokura, and M. Kawasaki, J. Phys. Soc. Jpn. **87**, 074704 (2018).
[12] Z. Zhang, P. Yang, M. Hong, S. Jiang, G. Zhao, J. Shi, Q. Xie, and Y. Zhang, Nanotechnology **30**, 182002 (2019).
[13] C. Gong and X. Zhang, Science **363**, eaav4450 (2019).
[14] G. I. Makovetskii and S. S. Dorofeichik, Inorg. Mater. **43**, 591 (2007).
[15] A. Ohsawa, Y. Yamaguchi, N. Kazama, H. Yamaguchi, and H. Watanabe, J. Phys. Soc. Jpn. **33**, 1303 (1972).
[16] T. Hirone and S. Chiba, J. Phys. Soc. Jpn. **15**, 1991 (1960).
[17] M. Yamaguchi and T. Hashimoto, J. Phys. Soc. Jpn. **32**, 635 (1972).
[18] T. Hashimoto, K. Hoya, M. Yamaguchi, and I. Ichitsubo, J. Phys. Soc. Jpn. **31**, 679 (1971).
[19] H. Ipser, L. K. Komarek, and K. O. Klepp, J. Less-Common Met. **92**, 265 (1983).
[20] K. Lukoschus, S. Kraschinski, C. Nather, W. Bensch, and R. K. Kremer, J. Solid State Chem. **177**, 951 (2004).
[21] Y. Wang, J. Yan, J. Li, S. Wang, M. Song, J. Song, Z. Li, K. Chen, Y. Qin, L. Ling, H. Du, L. Cao, X. Luo, Y. Xiong, and Y. Sun, Phys. Rev. B **100**, 024434 (2019).
[22] X. H. Luo, W. J. Ren, and Z. D. Zhang, J. Magn. Magn. Mater. **445**, 37 (2018).
[23] D. C. Freitas, R. Weht, A. Sulpice, G. Remenyi, P. Strobel, R. Gay, J. Marcus, and M. N. Regueiro, J. Phys.: Condens. Matter **27**, 176002 (2015).
[24] J. Yan, X. Luo, G. Lin, F. Chen, J. Gao, Y. Sun, L. Hu, P. Tong, W. Song, Z. Sheng, W. Lu, X. Zhu, and Y. Sun, Europhys. Lett. **124**, 67005 (2018).
[25] X. Sun, W. Li, X. Wang, Q. Sui, T. Zhang, Z. Wang, L. Liu, D. Li, S. Feng, S. Zhong, H. Wang, V. Bouchiat, M. N. Regueiro, N. Rougemaille, J. Coraux, Z. Wang, B. Dong, X. Wu, T. Yang, G. Yu, B. Wang, Z. V. Han, X. Han, and Z. Zhang, Nano Res. **13**, 3358 (2020).
[26] Y. Wen, Z. Liu, Y. Zhang, C. Xia, B. Zhai, X. Zhang, G. Zhai, C. Shen, P. He, R. Cheng, L. Yin, Y. Yao, M. Sendeku, Z. Wang, X. Ye, C. Liu, C. Jiang, C. Shan, Y. Long, and J. He, Nano Lett. **20**, 3130 (2020).
[27] T. Hamasaki, T. Hashimoto, Y. Yamaguchi, and H. Watanabe, Solid State Commun. **16**, 895 (1975).
[28] A. F. Andersen, Acta Chem. Scand. **24**, 3495 (1970).
[29] S. Polesya, S. Mankovsky, D. Benea, H. Ebert, and W. Bensch, J. Phys.: Condens. Matter **22**, 156002 (2010).
[30] G. Cao, Q. Zhang, M. Frontzek, W. Xie, D. Gong, G. E. Sterbinsky, and R. Jin, Phys. Rev. Mater. **3**, 125001 (2019).
[31] A. Roy, S. Guchhait, R. Dey, T. Pramanik, C. C. Hsieh, A. Rai, and S. K. Banerjee, ACS Nano **9**, 3772 (2015).
[32] L. Zhou, J. S. Chen, Z. Z. Du, X. S. He, B. C. Ye, G. P. Guo, H. Z. Lu, G. Wang, and H. T. He, AIP Adv. **7**, 125116 (2017).
[33] T. Pramanik, A. Roy, R. Dey, A. Rai, S. Guchhait, H. C. P. Movva, C. C. Hsieh, and S. K. Banerjee, J. Magn. Magn. Mater. **437**, 72 (2017).
[34] D. M. Burn, L. B. Duffy, R. Fujita, S. L. Zhang, A. I. Figueroa, J. H. Martin, G. van der Laan, and T. Hesjedal, Sci. Rep. **9**, 10793 (2019).
[35] H. Li, L. Wang, T. Yu, L. Zhou, Y. Qiu, H. He, F. Ye, I. K. Sou, and G. Wang, ACS Appl. Nano Mater. **2**, 6809 (2019).
[36] D. Zhao, L. Zhang, I. A. Malik, K. Liao, W. Cui, X. Cai, C. Zheng, L. Li, X. Hu, D. Zhang, X. Chen, X. Jiang, and Q. Xue, Nano Res. **11**, 3116 (2018).
[37] J. Chen, L. Wang, M. Zhang, L. Zhou, R. Zhang, L. Jin, X. Wang, H. Qin, Y. Qiu, J. Mei, F. Ye, B. Xi, H. He, B. Li, and G. Wang, Nano Lett. **19**, 6144 (2019).
[38] L. Zhou, J. Chen, X. Chen, B. Xi, Y. Qiu, J. Zhang, L. Wang, R. Zhang, B. Ye, P. Chen, X. Zhang, G. Guo, D. Yu, J. W. Mei, F. Ye, G. Wang, and H. He, ACS Appl. Mater. Interfaces **12**, 25135 (2020).
[39] See Supplemental Material at http://link.aps.org/supplemental/10.1103/PhysRevMaterials.4.114001 for additional details regarding growth procedure, XRD, magnetization data analysis, XMCD data analysis, and theoretical calculations.
[40] R. Laskowski, G. K. H. Madsen, P. Blaha, and K. Schwarz, Phys. Rev. B **69**, 140408(R) (2004).
[41] J. Kunes and R. Laskowski, Phys. Rev. B **70**, 174415 (2004).
[42] P. Blaha, K. Schwarz, F. Tran, R. Laskowski, G. K. H. Madsen, and L. D. Marks, J. Chem. Phys. **152**, 074101 (2020).

[43] J. P. Perdew, K. Burke, and M. Ernzerhof, Phys. Rev. Lett. **77**, 3865 (1996).
[44] J. Rusz, L. Bergqvist, J. Kudrnovský, and I. Turek, Phys. Rev. B **73**, 214412 (2006).
[45] L. M. Sandratskii, Adv. Phys. **47**, 91 (1998).
[46] Y. Okada, Y. Ando, R. Shimizu, E. Minamitani, S. Shiraki, S. Watanabe, and T. Hitosugi, Nat. Commun. **8**, 15975 (2017).
[47] M. Nakano, Y. Wang, S. Yoshida, H. Matsuoka, Y. Majima, K. Ikeda, Y. Hirata, Y. Takeda, H. Wadati, Y. Kohama, Y. Ohigashi, M. Sakano, K. Ishizaka, and Y. Iwasa, Nano Lett. **19**, 8806 (2019).
[48] M. Nakano, Y. Wang, Y. Kashiwabara, H. Matsuoka, and Y. Iwasa, Nano Lett. **17**, 5595 (2017).
[49] Y. Umemoto, K. Sugawara, Y. Nakata, T. Takahashi, and T. Sato, Nano Res. **12**, 165 (2019).
[50] R. Watanabe, R. Yoshimi, M. Shirai, T. Tanigaki, M. Tsukazaki, K. S. Takahashi, R. Arita, M. Kawasaki, and Y. Tokura, Appl. Phys. Lett. **113**, 181602 (2018).
[51] A. R. Denton and N. W. Ashcroft, Phys. Rev. A **43**, 3161 (1991).
[52] M. T. Johnson, P. J. H. Bloemen, F. J. A. den Broeder, and J. J. de Vries, Rep. Prog. Phys. **59**, 1409 (1996).
[53] K. Yaji, A. Kimura, C. Hirai, M. Taniguchi, M. Koyama, H. Sato, K. Shimada, A. Tanaka, T. Muro, S. Imada, and S. Suga, Phys. Rev. B **70**, 064402 (2004).
[54] K. Yaji, A. Kimura, M. Koyama, C. Hirai, H. Sato, K. Shimada, A. Tanaka, and M. Taniguchi, J. Appl. Phys. **97**, 10A316 (2005).
[55] B. T. Thole, P. Carra, F. Sette, and G. van der Laan, Phys. Rev. Lett. **68**, 1943 (1992).
[56] P. Carra, B. T. Thole, M. Altarelli, and X. Wang, Phys. Rev. Lett. **70**, 694 (1993).
[57] K. T. Ko, K. Kim, S. B. Kim, H. D. Kim, J. Y. Kim, B. I. Min, J. H. Park, F. H. Chang, H. J. Lin, A. Tanaka, and S. W. Cheong, Phys. Rev. Lett. **107**, 247201 (2011).
[58] N. Majlis, *The Quantum Theory of Magnetism* (World Scientific, Singapore, 2007), Chap. 3.
[59] B. Dupé, M. Hoffmann, C. Paillard, and S. Heinze, Nat. Commun. **5**, 4030 (2014).
[60] T. Kurumaji, T. Nakajima, M. Hirschberger, A. Kikkawa, Y. Yamasaki, H. Sagayama, H. Nakao, Y. Taguchi, T. H. Arima, and Y. Tokura, Science **365**, 914 (2019).
[61] K. Monna and F. Izumij, J. Appl. Crystallogr. **44**, 1272 (2011).